Acta Crystallographica Section D
Biological Crystallography
ISSN 0907-4449

Reduction of X-ray-induced radiation damage of macromolecular crystals by data collection at 15 K: a systematic study

A. Meents,[a]*‡ A. Wagner,[b]*‡ R. Schneider,[a] C. Pradervand,[a] E. Pohl[a] and C. Schulze-Briese[a]

[a]Paul Scherrer Institut, Swiss Light Source, CH-5232 Villigen, Switzerland, and [b]Diamond Light Source Ltd, Chilton, Didcot OX11 0DE, England

‡ These authors contributed equally to this work.

Correspondence e-mail: alke.meents@psi.ch, armin.wagner@diamond.ac.uk

Received 4 September 2006
Accepted 8 December 2006

The cryocooling of protein crystals to temperatures of around 100 K drastically reduces X-ray-induced radiation damage. The majority of macromolecular data collection is therefore performed at 100 K, yielding diffraction data of higher resolution and allowing structure determination from much smaller crystals. However, at third-generation synchrotron sources radiation damage at 100 K still limits the useful data obtainable from a crystal. For data collection at 15 K, realised by the use of an open-flow helium cryostat, a further reduction of radiation damage is expected. However, no systematic studies have been undertaken so far. In this present study, a total of 54 data sets have been collected from holoferritin and insulin crystals at 15 and 90 K in order to identify the effect of the lower data-collection temperature on the radiation damage. It is shown that data collection at 15 K has only a small positive effect for insulin crystals, whereas for holoferritin crystals radiation damage is reduced by 23% compared with data collection at 90 K.

1. Introduction

Macromolecular crystallography beamlines at third-generation synchrotrons can easily achieve photon fluxes greater than 10^{12} photons s^{-1}, with micro-focusing optics allowing this flux to be delivered on spots of 50 μm^2 or smaller. Because of this immense flux density and the resulting large absorbed dose, radiation damage has become an important factor in successful macromolecular structure determination (Garman & Nave, 2002). The cooling of protein crystals to cryogenic temperatures drastically reduces the rate of damage to the crystals (Blake & Phillips, 1962; Low *et al.*, 1966). Following the introduction of appropriate freezing techniques and cryostats (Haas & Rossmann, 1970; Garman & Schneider, 1997; Teng, 1990), data collections are now routinely performed at 90–120 K using open-flow nitrogen cryostats. However, even at temperatures of around 100 K radiation damage is still a major obstacle to successful structure determination. Especially for systems yielding only small crystals or with large unit cells, a further mitigation of radiation damage would therefore be highly desirable.

Cryocooling of biological samples to lower temperatures than 90 K has been discussed for many years in cryo-electron microscopy. In electron-microscopy studies of two-dimensional bacteriorhodopsin crystals, Stark and coworkers found a 'cryoprotection factor' of 1.4 for the low-resolution shell data (7 Å) and of 2.5 for the high-resolution shell data (2.5 Å; Stark *et al.*, 1996) on decreasing the data-collection temperature from 98 to 4 K. However, detrimental effects of cooling to 12 K compared with 82 K have more recently been observed in cryo-electron tomography (Iancu *et al.*, 2006). The

authors postulate that vitreous ice present at 12 K undergoes a phase transition upon electron irradiation, leading to a volume expansion and thereby destroying the sample.

Open-flow helium cryostats allow data collection at temperatures as low as 5 K without additional scattering arising from vacuum windows, as is the case with closed-cycle cryostats. Experiments with two D-xylose isomerase crystals revealed a longer lifetime of the crystal exposed to an intense X-ray beam at 17 K compared with that at 100 K (Hanson *et al.*, 2002). In a second study, a weak positive effect of cooling to 40 K was found for hen egg-white lysozyme crystals at high absorbed doses (Teng & Moffat, 2002).

However, to date no systematic studies comparing a large number of crystals have been undertaken. It is therefore the goal of this study to systematically investigate the effect of cryocooling to 15 K on radiation damage to protein crystals. Therefore, additional parameters such as initial crystal quality, effects of crystal handling and cryocooling protocol and data-collection parameters have been minimized. Furthermore, a control experiment at 90 K using an identical experimental setup was performed (with the exception of using an N_2 crysotat instead of a He cryostat). The comparison of a large number of crystals should lead to statistically reliable results.

2. Experimental

Porcine insulin and horse spleen holoferritin were chosen as model systems for a number of reasons. Both proteins can be easily and reproducibly crystallized, yielding crystals of comparable size and quality. Furthermore, they can be crystallized in the cubic crystal system. This facilitates subsequent data evaluation, since crystal rotations of less than 30° are sufficient to obtain almost complete data sets with sufficient redundancy for significant statistics. Additionally, crystallization conditions containing the cryoprotectant were available for both proteins. This eliminates possible variations in crystal quality arising from additional cryo-handling steps, *e.g.* slightly different soaking times.

A further reason for choosing holoferritin as a model system was its high absorption cross-section. This is mainly a consequence of its amorphous iron core, which contains around 1760 Fe atoms (Owen *et al.*, 2006).

2.1. Crystallization

The crystallization of proteins depends on many physical and chemical parameters such as changes of temperature, pH, protein and precipitate concentration (McPherson, 2002). It is of advantage if the contribution of crystal quality variations to the X-ray data quality is smaller than the expected effect of cryocooling from 90 to 15 K. Therefore, only crystals grown under the same conditions were used for the experiment.

Cubic Zn-free insulin crystals (space group $I2_13$; unit-cell parameter $a \simeq 78$ Å; molecular weight 5.8 kDa; 65% solvent content) were grown by batch crystallization by mixing 3 µl 15 mg ml^{-1} porcine insulin (Sigma Aldrich, catalogue No. I-5523) solution in 0.05 *M* sodium phosphate buffer pH 11 with 3 µl 25%(*v*/*v*) ethylene glycol solution in the same buffer. Crystals grew in around one week to 60–100 µm in size. Holoferritin crystals (space group *F*432; unit-cell parameter $a \simeq 181$ Å; molecular weight 19.8 kDa; 64% solvent content) were grown by mixing equal amounts of a 10 mg ml^{-1} aqueous ferritin solution (Fluka, catalogue No. 96701) with a reservoir solution containing 80 m*M* $CdSO_4$, 0.8 *M* $(NH_4)_2SO_4$ and 25%(*v*/*v*) glycerol and subsequent equilibration against this reservoir solution (Ravelli *et al.*, 2002). Crystals with dimensions of 75–125 µm grew within a few days. Insulin and ferritin crystals with average dimensions in the range 80–100 µm were chosen for the experiments.

Table 1
Summary of insulin and ferritin data-collection parameters at beamline X10SA at the Swiss Light Source (SLS).

The photon flux at 13.5 keV was experimentally determined to be 1.8×10^{12} photons s^{-1}.

	Oscillation range (°)	Exposure time (s)	No. of images	Dose per image (Gy)	Crystal-to-detector distance (mm)
Insulin	1	1	360	0.74×10^5	120
Ferritin	0.5	1	270	3.1×10^5	140

2.2. Beamline setup

At third-generation synchrotron sources, the beam size is often smaller than the crystal cross-section. Rotation of the crystal during data collection causes unexposed and therefore undamaged crystal material to be continuously introduced into the beam. Thus, a more or less damaged part and a completely undamaged part contribute to the diffraction pattern (Schulze-Briese *et al.*, 2005). This dramatically complicates subsequent analysis of radiation-damage effects. To eliminate these volume effects and to expose the whole crystal in the vertical direction perpendicular to the rotation axis, the beam was vertically defocused to a size of 200 × 80 µm (vertical × horizontal). The beamsize was adjusted by viewing a cerium-doped YAG screen with a video camera. This ensured that all crystals were bathed in the beam in a vertical direction (perpendicular to the rotation axis) during the experiments.

Data collection at 15 K was performed using an open-flow helium cryostat (HeliJet) from Oxford Diffraction. Prior to protein data collection, the temperature of the device was calibrated with a Si diode (Lakeshore DT-421-HR) at both room temperature and 10 K. Additionally, the cubic to hexagonal phase transition of $Ni(NH_3)_6I_2$ occurring at around 19.7 K was used to validate the temperature calibration from diffraction images (Eckert & Press, 1980). The HeliJet consumed around 2 l of liquid helium per hour when operated at 15 K during the experiments, which corresponds to a gas-flow rate of 25 l min^{-1} (for the inner and outer shield together). The corresponding data collections at 90 K were realised using a standard open-flow nitrogen cryostat (CryoJet) from Oxford Instruments. The flow rates were adjusted to 10 l min^{-1} each for the inner and outer shield. To facilitate crystal centring, especially when using the HeliJet, an

Table 2
Summary of insulin data-set statistics at 15 and 90 K.

The first value in each cell is the average value over all data sets. The following values in parentheses are the lowest and highest values found within the corresponding group.

	Insulin, 15 K (first data sets)	Insulin, 15 K (last data sets)	Insulin, 90 K (first data sets)	Insulin, 90 K (last data sets)
$\langle I/\sigma(I)\rangle$	16.18 (12.26, 19.99)	11.97 (9.37, 14.59)	17.81 (14.68, 21.11)	13.50 (9.15, 18.18)
$\langle R_{\rm sym}\rangle$	5.6 (4.3, 8.9)	6.5 (5.1, 9.8)	4.9 (4.2, 5.6)	5.5 (4.1, 6.8)
⟨Completeness⟩	93.3 (88.8, 97.0)	92.6 (86.7, 94.9)	93.5 (85.9, 96.8)	92.5 (88.6, 94.0)
⟨Redundancy⟩	3.7 (3.6, 3.9)	3.6 (3.0, 3.9)	3.8 (3.7, 3.9)	3.6 (2.8, 3.8)
$\langle I/\sigma(I)\rangle$, 1.5–2.0 Å	9.87 (5.32, 13.31)	4.35 (1.95, 7.11)	11.35 (6.70, 17.57)	4.33 (2.16, 7.88)
$\langle R_{\rm sym}\rangle$, 1.5–2.0 Å	12.5 (7.9, 24.5)	35.3 (14.2, 70.8)	10.5 (5.5, 18.2)	35.5 (14.6, 64.8)
⟨Completeness⟩, 1.5–2.0 Å	95.4 (88.1, 99.3)	91.0 (83.7, 97.1)	96.4 (92.7, 99.0)	90.4 (84.8, 96.0)
⟨Redundancy⟩, 1.5–2.0 Å	3.8 (3.7, 4.1)	3.8 (2.9, 4.1)	3.7 (3.6, 3.9)	3.8 (2.9, 4.1)
Wilson *B* factor (Å^2)	15.1 (11.9, 16.8)	22.2 (19.9, 24.3)	15.2 (12.8, 16.4)	22.4 (20.5, 23.6)
Lattice spacing (Å)	77.33 (77.14, 77.48)	77.62 (77.47, 77.78)	77.43 (77.34, 77.57)	77.62 (77.47, 77.75)
Mosaicity (°)	0.20 (0.12, 0.26)	0.21 (0.11, 0.30)	0.14 (0.09, 0.17)	0.16 (0.10, 0.29)
Total dose (MGy)	2.2	26.6	2.2	26.6

on-axis viewing system was installed at the beamline. All crystals were flash-cooled by moving them quickly into the cold stream of the corresponding cryostat.

2.3. Diffraction experiment

Diffraction experiments were carried out at the macromolecular crystallography beamline X10SA of the Swiss Light Source (SLS) at Paul Scherrer Institut, Villigen, Switzerland (Pohl *et al.*, 2006). All X-ray diffraction data were collected at a photon energy of 13.5 keV. A rotation increment of 1° was chosen for insulin and of 0.5° for holoferritin owing to its larger unit-cell parameters. Data-collection parameters for both the insulin and ferritin crystals are summarized in Table 1. All experiments were performed without any changes of beamline parameters, thereby guaranteeing the same data-collection conditions for all crystals, apart from the data-collection temperature. The SLS storage ring is routinely operated in TOPUP mode with beam-intensity variations of less than 0.5%, thus no corrections for the ring-induced decay of the primary beam intensity were required. The incident photon flux was monitored by using a PIN diode and the beam position was monitored using a CVD diamond quadrant beam-position monitor (Schulze-Briese *et al.*, 2001). No changes of flux or position were observed over the 72 h of the experiments. All data were collected with the same exposure time of 1 s per rotation increment. This procedure yields a continuous series of images and excludes any possible dose-rate effects on radiation damage (Leiros *et al.*, 2006; Ravelli *et al.*, 2003). The disadvantages of this approach are longer data-collection times per crystal for the same total dose and more saturated (low-order) reflections.

Data sets were collected from 26 insulin crystals and 28 ferritin crystals; for each crystal type, half of these data sets were collected at 15 K and half at 90 K.

2.4. Data processing

The diffraction images were subsequently processed using the program package *XDS* (Kabsch, 2001) in two different ways. Data were integrated in 30° wedges for the insulin crystals and in 15° wedges for the ferritin crystals. With total crystal rotations of 360° for insulin crystals and 135° for ferritin crystals, 12 consecutive data sets were obtained for every insulin crystal and nine consecutive data sets for every ferritin crystal. A total of 564 independently processed data sets were thus obtained. Only one of these data sets could not be used for further analysis owing to several blank images caused by shutter-synchronization errors. All insulin and ferritin data were processed and scaled in the same way. For high-resolution data (<2.0 Å), statistics were calculated in shells of 0.1 Å width. From these shells, the outermost shell with an average $I/\sigma(I)$ ratio of >6 was determined from the first wedge of data from each crystal. Statistical quality indicators such as the $I/\sigma(I)$ ratios or the $R_{\rm sym}$ values from this resolution shell were used throughout the paper to monitor radiation damage-induced decay in subsequent rotation wedges. As radiation-induced decay of diffraction properties, rather than the initial diffraction quality, is of primary interest, normalized data-quality indicators were calculated for analysis. These normalized parameters were obtained by dividing the data-quality indicators of the subsequent wedges by their values from the first wedge. The standard deviations shown as error bars in Figs. 2–5 are based on the scatter of these normalized parameters within each group. All data-set statistics were calculated with *XSCALE*. The resolution limit is defined as the resolution shell still providing a completeness of 50% at $I/\sigma(I) \geq 2$ (Sheldrick *et al.*, 1993).

In order to determine the unit-cell parameter more accurately, all data were reprocessed keeping the crystal-to-detector distance fixed, as data from the initial processing showed a significant shift in the crystal-to-detector distance. To obtain an indicator for the absolute crystal quality, all data were additionally scaled with a high-resolution limit of 1.5 Å for insulin and 1.8 Å for ferritin. To indicate the quality of the high-resolution data, a resolution shell of 1.5–2.0 Å (insulin) and 1.8–2.3 Å (ferritin) was chosen. Tables 2 and 3 give average and extreme absolute values for the first and last data wedge for several quality indicators.

Dose calculations were performed with the program *RADDOSE* (Murray *et al.*, 2004). Additionally, for the dose

Table 3
Summary of ferritin data-set statistics at 15 and 90 K.

The first value in each cell is the average value over all data sets. The following values in parentheses are the lowest and highest values found within the corresponding group.

	Ferritin, 15 K (first data sets)	Ferritin, 15 K (last data sets)	Ferritin, 90 K (first data sets)	Ferritin, 90 K (last data sets)
$\langle I/\sigma(I)\rangle$	15.32 (10.26, 20.65)	11.46 (8.28, 16.73)	21.76 (17.58, 26.00)	16.44 (12.30, 21.13)
$\langle R_{\rm sym}\rangle$	6.0 (4.4, 7.8)	7.8 (5.1, 10.8)	5.2 (3.4, 19.9)	6.5 (4.0, 24.5)
⟨Completeness⟩	84.9 (64.0, 95.2)	89.9 (79.8, 95.2)	90.9 (75.9, 96.4)	90.2 (77.1, 94.9)
⟨Redundancy⟩	3.9 (3.1, 5.1)	3.8 (2.9, 4.1)	3.7 (3.5, 4.5)	3.8 (3.6, 4.4)
$\langle I/\sigma(I)\rangle$, 1.8–2.3 Å	7.10 (3.75, 12.28)	4.04 (2.14, 6.90)	12.43 (8.73, 16.97)	6.40 (3.60, 10.25)
$\langle R_{\rm sym}\rangle$, 1.8–2.3 Å	12.5 (5.8, 23.3)	23.4 (11.9, 43.1)	6.4 (3.6, 10.3)	14.3 (7.1, 24.5)
⟨Completeness⟩, 1.8–2.3 Å	82.2 (63.4, 91.8)	84.6 (75.7, 91.1)	88.3 (79.1, 93.8)	85.5 (76.7, 92.7)
⟨Redundancy⟩, 1.8–2.3 Å	4.1 (3.2, 5.5)	4.1 (3.8, 5.2)	3.9 (3.6, 4.7)	4.1 (3.7, 4.8)
Wilson B factor (Å^2)	20.2 (16.6, 24.5)	27.9 (24.5, 31.8)	16.4 (14.9, 18.3)	25.8 (21.7, 34.8)
Lattice spacing (Å)	180.18 (179.79, 180.44)	180.86 (180.51, 181.27)	180.48 (180.13, 180.71)	181.03 (180.82, 181.58)
Mosaicity (°)	0.19 (0.13, 0.27)	0.18 (0.12, 0.29)	0.12 (0.08, 0.22)	0.13 (0.09, 0.19)
Total dose (MGy)	9.3	83.7	9.3	83.7

calculations of holoferritin, the core of 1760 Fe atoms per 24 protein subunits was included as recently determined by microPIXE (Owen *et al.*, 2006).

3. Results

Radiation damage in macromolecular crystals manifests itself in different ways. Most obvious to the experimentalist is the loss of diffraction power of the crystal. This degradation can be easily analyzed in a quantitative way by following the decay of various parameters. In particular, the decay of the relative $I/\sigma(I)$ values, the increase in $R_{\rm sym}$ and the decay of the resolution limit were used as diffraction data-quality indicators in order to follow radiation damage. In addition, changes in both the unit-cell parameter and the crystal mosaicity were analyzed. In addition to changes in the global diffraction quality, X-rays induce specific structural changes at certain specific sites (Weik *et al.*, 2000; Ravelli & McSweeney, 2000; Burmeister, 2000). The analysis of specific radiation damage at the two different data-collection temperatures is beyond the scope of this paper and will be discussed in a forthcoming paper.

3.1. Decay of diffracting power

Fig. 1 shows the decay of $I/\sigma(I)$ for the $I/\sigma(I) > 6$ shell as function of the absorbed dose for all measured crystals. Fig. 2 shows a plot of the averaged normalized $I/\sigma(I)$ as a function of the absorbed dose for the two different data-collection temperatures. In order to allow a quantitative comparison, a linear function was fitted to both the ferritin and insulin data. The slope of the 15 K data sets is significantly smaller than for the 90 K data in the case of ferritin, whereas for insulin only a small difference is found. The slopes of the fit function show a small reduction of the $I/\sigma(I)$ decay of 6% in the case of insulin (-0.0218 ± 0.0005 *versus* -0.0231 ± 0.0008 MGy^{-1}; accumulated dose 26.64 MGy) and a significant reduction of 23% for holoferritin (-0.0056 ± 0.0001 *versus* -0.0073 ± 0.0002 MGy^{-1}; accumulated dose 83.7 MGy). The absolute overall values of $I/\sigma(I)$ show a small difference in the starting values of the 15 and 90 K data sets for the insulin crystals: 16.2 $\pm$ 2.0 at 15 K and 17.81 $\pm$ 2.0 at 90 K. The initial $I/\sigma(I)$ ratios for the ferritin crystals are 15.3 $\pm$ 3.0 for the 15 K data and 21.8 $\pm$ 2.5 for the 90 K data. These unexpected differences are probably a result of the flash-cooling protocol and will be discussed later.

In addition to the differing behaviour of the two proteins with respect to the reduction of radiation damage when lowering the data-collection temperature, insulin and ferritin also differ drastically in their total susceptibility to radiation damage. In the case of insulin $I/\sigma(I)$ is reduced to 50% of its initial value in the outermost resolution shells, providing an $I/\sigma(I) \geq 6$ after an absorbed dose of 22 MGy (90 K) and 24 MGy (15 K), whereas for ferritin the same reduction is observed only after a dose of 77 MGy (90 K) and can be extrapolated to 99 MGy for 15 K, respectively.

Other overall data-quality parameters such as the $R_{\rm sym}$ values and the resolution limit follow the same trend as $I/\sigma(I)$. The increase of the relative $R_{\rm sym}$ values with dose is shown in Fig. 3. A positive effect of cryocooling to 15 K can clearly be seen in both cases. As already observed for the $I/\sigma(I)$, this positive effect is more pronounced in the case of ferritin. The averaged absolute $R_{\rm sym}$ value for the insulin crystals increases from 19.1 $\pm$ 2.7% to 46.0 $\pm$ 4.6% for the 15 K data and from 19.5 $\pm$ 1.8 to 50.9 $\pm$ 3.6% for the 90 K data. For ferritin an increase from 20.7 $\pm$ 1.6% to 38.3 $\pm$ 4.4% at 15 K and from 18.5 $\pm$ 2.0% to 45.2 $\pm$ 6.1% at 90 K is observed.

Fig. 4 shows the absolute decrease of the averaged resolution limits for insulin and ferritin at the two different temperatures as a function of absorbed dose. The insulin crystals at 15 and 90 K start with almost the same average resolution limit: 1.35 $\pm$ 0.06 and 1.36 $\pm$ 0.09 Å, respectively. These values decrease to 1.58 $\pm$ 0.13 Å at 15 K and to 1.61 $\pm$ 0.11 Å at 90 K in the last wedge. Thus, only a small reduction in radiation damage-induced decay is observed in the resolution limit for insulin. For the ferritin crystals the initial resolution limit for the 15 K crystal (1.78 $\pm$ 0.19 Å) is almost 0.3 Å lower than for the 90 K crystals (1.50 $\pm$ 0.09 Å). During dose accumulation, the resolution limit decreases by 0.17 Å to 1.95 $\pm$ 0.14 Å at 15 K and by 0.31 Å to a final value of 1.81 $\pm$

0.10 Å at 90 K. As previously mentioned, the differences in the initial crystal quality are probably a consequence of the different gases and temperature gradients used for flash-cooling. However, for the 15 K data a much slower decrease of the resolution limit with dose is observed, indicating a reduced damage rate compared with the 90 K data, as already observed for the $I/\sigma(I)$ ratio and the $R_{\rm sym}$ values.

3.2. Crystal mosaicity

An increase in the crystal mosaicity arising from radiation damage has been previously observed in protein crystals (Ravelli *et al.*, 2002; Ravelli & McSweeney, 2000). However, in the present study no significant changes could be found. Insulin crystals flash-frozen at 15 and 90 K show average mosaicities of 0.20 ± 0.04 and 0.14 ± 0.03° in the first wedge, increasing to 0.21 ± 0.05 and 0.16 ± 0.05°, respectively. The average mosaicity of ferritin crystals at 15 K is 0.19 ± 0.04° in the first wedge, decreasing to 0.18 ± 0.05° in the last wedge, and increasing from 0.12 ± 0.04° to 0.13 ± 0.03° at 90 K. More notable than the mosaicity changes with X-ray dose are the differences between the two temperatures. In both cases, crystals flash-cooled in the 15 K helium gas stream show significantly higher mosaicity than crystals flash-frozen at 90 K.

The crystal mosaicities were taken from *XDS* data processing. It should be noted that the mosaicity parameters determined by *XDS*, or any other integration program, are not only sensitive to the crystal mosaicity itself, but are also affected by several other parameters. However, by using the same experimental conditions, the only variable is the crystal mosaicity. Therefore, these values should be considered as a relative measure rather than describing the 'real' crystal mosaicity, defined as the angular misalignment of the different mosaic blocks. The mosaicity values given should be well suited for indicating relative differences in the crystal quality.

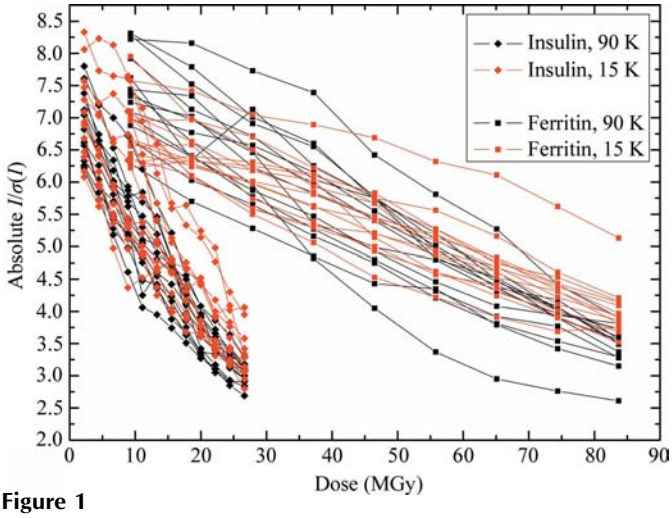

Figure 1
Decay of the absolute $I/\sigma(I)$ (see §2.4 for definition) for all insulin and ferritin crystals at 15 and 90 K plotted as a function of the absorbed dose.

3.3. Lattice parameters

In several previous studies, changes in the lattice parameters have been used to follow radiation damage (Müller *et al.*, 2002; Ravelli *et al.*, 2002). As expected, in the present study both proteins show smaller average starting lattice parameters at 15 K compared with at 90 K owing to reduced thermal motion. Insulin crystals show an average lattice parameter of 77.33 ± 0.10 Å at 15 K and 77.43 ± 0.06 Å at 90 K in the first wedge. These increase to values of 77.62 ± 0.10 Å at 15 K and 77.61 ± 0.08 Å at 90 K in the last wedge. The same trend is observed for ferritin: the averaged lattice parameters at 15 K are 180.2 ± 0.2 Å and 180.5 ± 0.2 Å at 90 K in the first wedge, increasing to 180.9 ± 0.2 Å (15 K) and 181.1 ± 0.2 Å (90 K) in the last wedge. Fig. 5 shows the relative increase of the lattice parameters for insulin and ferritin crystals as a function of

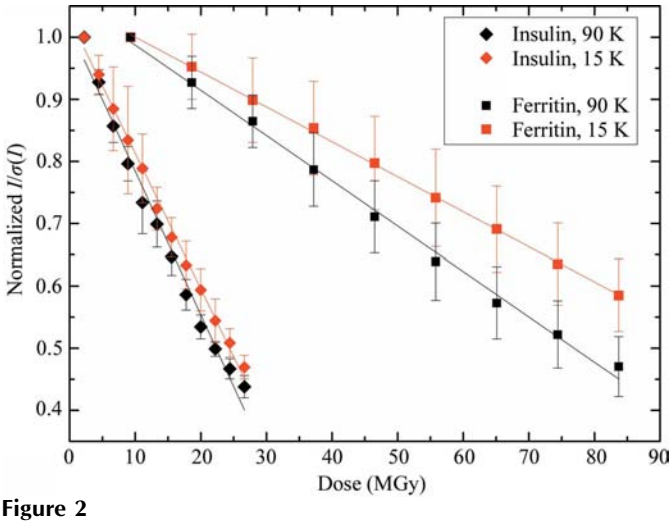

Figure 2
Decay of the normalized average $I/\sigma(I)$ (see §2.4 for definition) for insulin and ferritin crystals at 15 and 90 K plotted as a function of the absorbed dose. The corresponding linear-fit parameters for the graphs are given in the text.

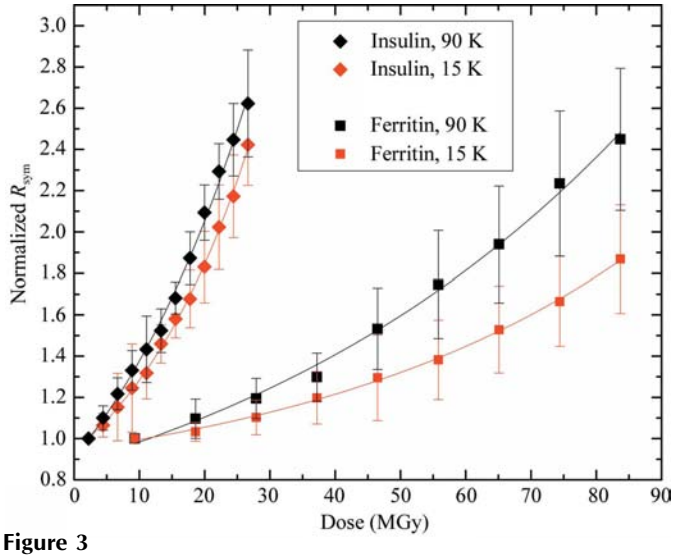

Figure 3
Average increase of the normalized $R_{\rm sym}$ for insulin and ferritin crystals measured at 15 and 90 K with dose. For both systems, an exponential growth of the $R_{\rm sym}$ values can be observed.

accumulated dose at the two different temperatures. Interestingly, in both cases a greater increase in the lattice parameters is observed at lower temperatures. In the case of insulin, the averaged lattice parameter at 15 K even attains a higher absolute value compared with the 90 K data in the last wedge.

4. Discussion

The analysis of $I/\sigma(I)$ ratios, $R_{\rm sym}$ values and resolution limits (Figs. 1–5) give a very consistent picture for the two proteins under study. For both insulin and holoferritin, a reduction of radiation damage at 15 K in comparison to 90 K is observed. Interestingly, the two model systems show different behaviour in the extent of this reduction. For insulin, the differences in the relative decay of $I/\sigma(I)$ at the two different temperatures are small (around 6%). Holoferritin presents a different picture: the reduction is much more pronounced and the difference in the decay of $I/\sigma(I)$ reaches 23%. The reason for this reduced radiation-damage rate is probably the slower diffusion of electrons and electron holes at lower temperatures. An explanation of the differences in the reduction of radiation damage between insulin and ferritin crystals might involve the pH-dependency of radiation chemistry; insulin was crystallized at pH 11 and ferritin at a pH of ∼7.

4.1. Crystal mosaicity

In addition to this reduced damage rate at 15 K compared with 90 K, ferritin crystals measured at 15 K clearly showed poorer initial diffraction properties. Differences in the initial absolute crystal-quality parameters such as $I/\sigma(I)$, $R_{\rm sym}$ values and resolution limit are probably the result of using different gases at different temperatures for flash-cooling (Kriminski *et al.*, 2003). It is well documented that the flash-cooling of protein crystals induces strain and stress within crystals, resulting in a higher crystal mosaicity compared with crystals at room temperature (Lovelace *et al.*, 2006). The strain and stress induced in the crystal would be more severe for higher temperature gradients. Therefore, one would expect a higher mosaicity for crystals flash-frozen in a 15 K helium stream compared with those flash-cooled to 90 K in gaseous nitrogen. This hypothesis is supported by the observation that insulin and ferritin crystals flash-cooled in the helium stream show a significantly higher mosaicity than crystals flash-cooled to 90 K. Insulin crystals flash-frozen to 15 K showed an average mosaicity that was 43% higher compared with those flash-cooled at 90 K. For ferritin a 38% higher mosacity was observed at 15 K. For the ferritin crystals at least, these higher mosaicity crystals at 15 K show poorer diffraction properties in terms of $I/\sigma(I)$ and $R_{\rm sym}$ compared with the 90 K crystals (Fig. 1, Table 3). This relation is also found for the insulin data, but is considerably less pronounced (Fig. 1, Table 2).

4.2. Sample vibrations

Another possible explanation of the differences in the data quality at 15 and 90 K could be sample vibrations induced by turbulence from the different cryostreams. Especially at protein crystallography undulator beamlines at third-generation synchrotron sources, which provide a very brilliant X-ray beam, such sample vibrations can result in poor data quality (Flot *et al.*, 2006). If the helium stream induces more sample vibrations than the nitrogen stream, then the quality of both low-resolution and high-resolution reflections should be affected, resulting in a decrease of $I/\sigma(I)$ and an increase in R values. In the present study, insulin and ferritin crystals measured at 15 and 90 K show comparable R values in the low-resolution shells. This indicates that the lower $I/\sigma(I)$ observed at 15 K is not a result of sample vibrations in the helium stream.

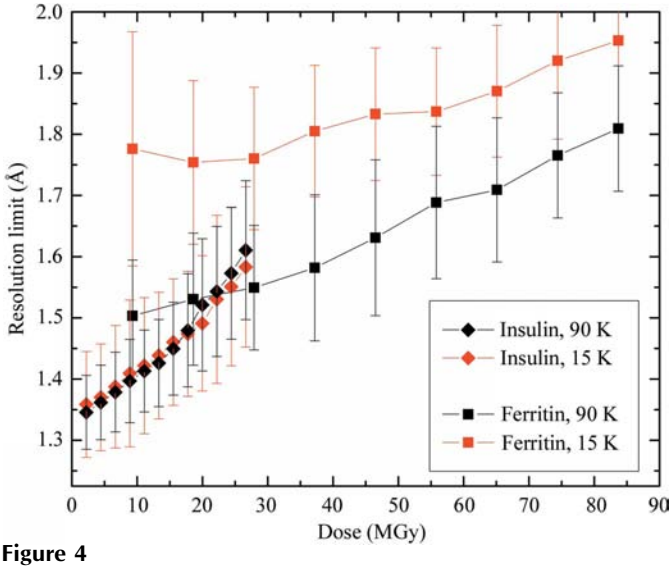

Figure 4
Decrease of the average resolution limit for insulin and ferritin crystals measured at 15 and 90 K with dose. The resolution limit is defined as the resolution shell that still provides a completeness of 50% at $I/\sigma(I) \geq 2$.

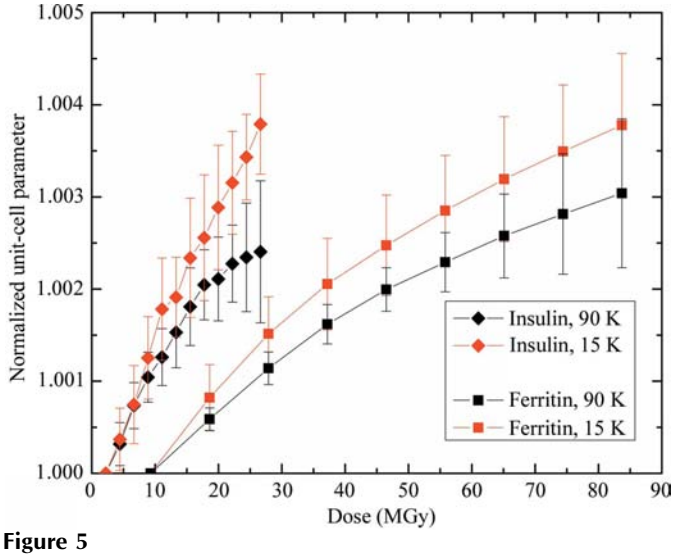

Figure 5
Averaged changes of the normalized unit-cell parameters of insulin and ferritin crystals at the two different data-collection temperatures of 15 and 90 K as a function of dose.

4.3. Lattice parameters

For both insulin and ferritin, an increase in the lattice parameter is observed as a function of dose. However, as already mentioned above, the magnitude of the increase surprisingly differs significantly at the two temperatures. At 15 K both systems show a significantly larger increase of their normalized lattice parameters compared with the crystals at 90 K. A possible explanation for this may be related to the gas which is generated as a result of irradiation with X-rays. This gas is observed to diffuse from cryocooled crystals when warming the crystal to room temperature following data collection. In room-temperature data collection such gas release is not observed owing to continuous diffusion of the gas out of the crystal. At 90 K, where diffusion is much slower, it at least partly remains in the crystal. At 15 K one would expect even lower diffusion coefficients than at 90 K. Thus, for the same dose rate more gas remains inside the crystal at 15 K compared with 90 K. The formation of gas inside the solvent channels would cause the unit cell to expand, leading at a later stage to cracks in the crystals and thereby increasing the mosaicity. If a greater volume of gas is retained in crystals at 15 K one would expect a steeper incline of the lattice parameters at 15 K compared with at higher temperatures. This behaviour can be observed for both systems, as shown in Fig. 5.

4.4. Susceptibility

It is interesting to compare the different damage rates of insulin and ferritin crystals as a function of the absorbed dose for both temperatures, as shown in Fig. 2. According to the dose-limit approach, comparable damage rates for different proteins with dose are to be expected (Henderson, 1990; Owen *et al.*, 2006). For insulin crystals $I/\sigma(I)$ fell to 50% of its initial value at an accumulated dose of 24 MGy (15 K) and 22 MGy (90 K). However, holoferritin crystals tolerate much higher doses. In the present study, doses of 99 MGy (15 K) and 77 MGy (90 K, extrapolated) were required to cause comparable signs of damage for ferritin crystals compared with insulin crystals (Figs. 1–3). Since all measurements were performed in one experimental run without any changes to the X-ray optics, beam-related effects should not have any impact on this observation. One explanation for this behaviour might be a different susceptibility to radiation damage of the two proteins.

Whereas insulin is a small globular protein with a composition that is typical for proteins, holoferritin is more exotic. Ferritin consists of a hollow sphere composed of 24 peptide subunits with an inner diameter of 78 Å, which in the case of horse spleen holoferritin is filled with an amorphous iron core composed of the mineral ferrihydrate $[FeO(OH)]_8[FeO(H_2PO_4)]$ containing about 1760 Fe atoms (Ford *et al.*, 1984; Owen *et al.*, 2006; Hempstead *et al.*, 1997). Owing to its amorphous nature, the iron core does not contribute to Bragg diffraction. However, with 72.6% of the total holoferritin absorption cross-section at 13.5 keV, the iron core contributes strongly to the absorption coefficient of holoferritin. Around 33% of the absorbed energy is released by *K*-shell X-ray fluorescence at an energy of 6.403 keV and around 67% as Auger electrons with energies between 550 and 650 eV. The inelastic mean free-path length of 600 eV Auger electrons in iron is less than 20 Å (Tanuma *et al.*, 1991). Hence, most of these Auger electrons will already be absorbed in the iron core and only a small fraction of them will reach the protein sphere and contribute to the specific damage there. This is in agreement with findings of Owen and coworkers, who found the first signs of specific radiation damage in holoferritin at residues located close to the iron core (Owen *et al.*, 2006). In ferrihydrate iron is in the oxidation state Fe^{III} (Ford *et al.*, 1984; Hempstead *et al.*, 1997), which is known for its high sensitivity to reduction (Beitlich *et al.*, 2007). This should further reduce the damage potential of the electrons released. To summarize, the iron core contributes strongly to the X-ray absorption cross-section, but secondary damage is also believed to be mainly restricted to this core. If the contribution of the iron core of holoferritin is excluded from the dose calculations, a total absorbed dose of 25.92 MGy is obtained for the ferritin after 270 s exposure. This value compares well to the total dose accumulated for the insulin crystals (26.64 MGy). Correcting for this in Figs. 1–5, one would obtain graphs superimposing on each other well at 90 K.

Another possible explanation for the differences in crystal susceptibilities could be the different cryoprotectants used. Glycerol and also ethylene glycol can act as radical scavengers (O'Neill *et al.*, 2002; Kauffmann *et al.*, 2006; Davydov *et al.*, 1994). Thus, the better scavenging capacities of glycerol in contrast to ethylene glycol could also contribute to the reduced damage rate observed for the ferritin crystals.

5. Conclusions

This work shows for the first time on a solid statistical basis that data collections at 15 K compared with 90 K can reduce radiation damage by around 6% for cubic insulin crystals and by 23% for holoferritin crystals. Additionally, holoferritin can tolerate three times the dose of insulin crystals before showing comparable signs of radiation damage. However, it should be noted that holoferritin, with its large amorphous iron core, has an unusual elemental composition for a protein. Thus, the extrapolation of the results from the holoferritin crystals to other proteins is limited. Moreover, the reduced damage rates observed for ferritin at 15 K may at least partly be related to the poorer initial crystal quality. For most proteins, one would therefore expect a behaviour similar to that described for insulin crystals. The reduced damage rate has to be compensated for by much greater experimental efforts and operational costs that are four to five times higher. Additionally, optimal flash-cooling procedures for cryocooling to 15 K need to be developed.

Summarizing the usefulness of data collection at 15 K for the reduction of radiation damage in the context of standard structure determinations in structural biology is quite limited. The fact that helium is a limited resource on earth has to be considered when thinking about performing data collections at 15 K with open-flow helium cryostats. However, extending

the temperature range accessible for X-ray data collection to temperatures down to 15 K might help in a few cases to reduce radiation damage. The main advantage of the cooling remains the ability to collect data at the highest possible resolution owing to lower *B* factors.

The HeliJet from Oxford Diffraction was a kind loan from Phil Pattison from the Swiss–Norwegian beamline and the on-axis viewing system was a loan from Joanne McCarthy, ESRF, Grenoble.

References

Beitlich, T., Kuehnel, K., Schulze-Briese, C., Shoeman, R. L. & Schlichting, I. (2007). *J. Synchrotron Rad.* **14**, 11–23.

Blake, C. F. F. & Phillips, D. C. (1962). *Biological Effects of Ionizing Radiation at the Molecular Level*, pp. 183–191. Vienna: IAEA.

Burmeister, W. P. (2000). *Acta Cryst.* D**56**, 328–341.

Davydov, R., Kuprin, S., Graslund, A. & Ehrenberg, A. (1994). *J. Am. Chem. Soc.* **116**, 11120–11128.

Eckert, J. & Press, W. (1980). *J. Chem. Phys.* **73**, 451–460.

Flot, D., Gordon, E. J., Hall, D. R., Leonard, G. A., McCarthy, A., McCarthy, J., McSweeney, S., Mitchell, E., Nurizzo, D., Ravelli, R. G. & Shepard, W. (2006). *Acta Cryst.* D**62**, 65–71.

Ford, G. C., Harrison, P. M., Rice, D. W., Smith, J. M., Treffry, A., White, J. L. & Yariv, J. (1984). *Philos. Trans. R. Soc. London Ser. B*, **304**, 551–565.

Garman, E. & Nave, C. (2002). *J. Synchrotron Rad.* **9**, 327–328.

Garman, E. F. & Schneider, T. R. (1997). *J. Appl. Cryst.* **30**, 211–237.

Haas, D. J. & Rossmann, M. G. (1970). *Acta Cryst.* B**26**, 998–1004.

Hanson, B. L., Harp, J. M., Kirschbaum, K., Schall, C. A., DeWitt, K., Howard, A., Pinkerton, A. A. & Bunick, G. J. (2002). *J. Synchrotron Rad.* **9**, 375–381.

Hempstead, P. D., Yewdall, S. J., Fernie, A. R., Lawson, D. M., Artymiuk, P. J., Rice, D. W., Ford, G. C. & Harrison, P. M. (1997). *J. Mol. Biol.* **268**, 424–448.

Henderson, R. (1990). *Proc. R. Soc. London Ser. B*, **241**, 6–8.

Iancu, C. V., Wright, E. R., Heymann, J. B. & Jensen, G. J. (2006). *J. Struct. Biol.* **153**, 231–240.

Kabsch, W. (2001). *International Tables for Crystallography*, Vol. *F*, edited by M. G. Rossmann & E. Arnold, ch. 11.3. Dordrecht: Kluwer Academic Press.

Kauffmann, B., Weiss, M. S., Lamzin, V. S. & Schmidt, A. (2006). *Structure*, **14**, 1099–1105.

Kriminski, S., Kazmierczak, M. & Thorne, R. E. (2003). *Acta Cryst.* D**59**, 697–708.

Leiros, H. K., Timmins, J., Ravelli, R. B. & McSweeney, S. M. (2006). *Acta Cryst.* D**62**, 125–132.

Lovelace, J. J., Murphy, C. R., Pahl, R., Brister, K. & Borgstahl, G. E. O. (2006). *J. Appl. Cryst.* **39**, 425–432.

Low, B. W., Chen, C. C., Berger, J. E., Singman, L. & Pletcher, J. F. (1966). *Proc. Natl Acad. Sci. USA*, **56**, 1746–1750.

McPherson, A. (2002). *Crystallization of Biological Macromolecules.* New York: Cold Spring Harbor Laboratory Press.

Müller, R., Weckert, E., Zellner, J. & Drakopoulos, M. (2002). *J. Synchrotron Rad.* **9**, 368–374.

Murray, J. W., Garman, E. F. & Ravelli, R. B. G. (2004). *J. Appl. Cryst.* **37**, 513–522.

O'Neill, P., Stevens, D. L. & Garman, E. F. (2002). *J. Synchrotron Rad.* **9**, 329–332.

Owen, R. L., Rudino-Pinera, E. & Garman, E. F. (2006). *Proc. Natl. Acad. Sci. USA*, **103**, 4912–4917.

Pohl, E., Pradervand, C., Schneider, R., Tomizaki, T., Pauluhn, A., Chen, Q., Ingold, G., Zimoch, E. & Schulze-Briese, C. (2006). *Synchrotron Radiat. News*, **19**, 24–26.

Ravelli, R. B. G., Leiros, H.-K. S., Pan, B., Caffrey, M. & McSweeney, S. (2003). *Structure*, **11**, 217–224.

Ravelli, R. B. G. & McSweeney, S. M. (2000). *Structure*, **8**, 315–328.

Ravelli, R. B. G., Theveneau, P., McSweeney, S. & Caffrey, M. (2002). *J. Synchrotron Rad.* **9**, 355–360.

Schulze-Briese, C., Ketterer, B., Pradervand, C., Bronnimann, C., David, C., Horisberger, R., Puig-Molina, A. & Graafsma, H. (2001). *Nucl. Instrum. Methods Phys. Res. A*, **467–468**, 230–234.

Schulze-Briese, C., Wagner, A., Tomizaki, T. & Oetiker, M. (2005). *J. Synchrotron Rad.* **12**, 261–267.

Sheldrick, G. M., Dauter, Z., Wilson, K. S., Hope, H. & Sieker, L. C. (1993). *Acta Cryst.* D**49**, 18–23.

Stark, H., Zemlin, F. & Boettcher, C. (1996). *Ultramicroscopy*, **63**, 75–79.

Tanuma, S., Powell, C. J. & Penn, D. R. (1991). *Surf. Interface Anal.* **17**, 927–939.

Teng, T.-Y. (1990). *J. Appl. Cryst.* **23**, 387–391.

Teng, T.-Y. & Moffat, K. (2002). *J. Synchrotron Rad.* **9**, 198–201.

Weik, M., Ravelli, R. B., Kryger, G., McSweeney, S., Raves, M. L., Harel, M., Gros, P., Silman, I., Kroon, J. & Sussman, J. L. (2000). *Proc. Natl Acad. Sci. USA*, **97**, 623–628.